Journal of Power Sources 248 (2014) 44–57

Contents lists available at ScienceDirect

Journal of Power Sources

journal homepage: www.elsevier.com/locate/jpowsour

2-D numerical modeling and experimental investigation of electrochemical mechanisms coupled with heat and mass transfer in a planar direct carbon fuel cell

Amal Elleuch [a], Melik Sahraoui [b], Ahlem Boussetta [a], Kamel Halouani [a, *], Yongdan Li [c]

[a] METS–ENIS, IPEIS, University of Sfax, Route Menzel Chaker Km 0.5, BP1172, 3018 Sfax, Tunisia
[b] LASMAP–EPT, University of Carthage, La Marsa, Tunis, Tunisia
[c] Tianjin Key Laboratory of Applied Catalysis Science and Technology, School of Chemical Engineering, University of Tianjin, Tianjin 30072, China

HIGHLIGHTS

- 2D computing model of electrochemistry coupled with mass and heat transfer in DCFC.
- Good agreement between numerical and experimental results (AAD of 9%).
- DCFC temperature distribution varied by 15 °C among all the cell sub-domains.
- Accurate prediction of DCFC polarization curve by using peroxide mechanism.
- DCFC output is sensitive to electrolyte porosity and anode specific surface area.

ARTICLE INFO

Article history:
Received 6 April 2013
Received in revised form
28 August 2013
Accepted 6 September 2013
Available online 20 September 2013

Keywords:
DCFC
Doped ceria
Modeling
Finite volume
Heat and mass transfer
Experimental validation

ABSTRACT

A two-dimensional modeling of a lab-scale planar Direct Carbon Fuel Cell (DCFC) of 20 mm in diameter is developed by taking into account of the electrochemical mechanisms and mass and heat transfer phenomena in all regions of the cell simultaneously. The electrodes and the electrolyte of the DCFC are both considered as distinct regions with different local properties such as permeability, conductivity and diffusivity. An improved packed bed anodic structure with a finite thickness is also adopted. General boundary conditions are implemented by taking into consideration the species concentrations at the DCFC inlet such as oxygen concentration which is a very important parameter to determine the cell efficiency. The effects of the main operating parameters such as temperature, inlet gas flow velocity and porosity of the electrolyte matrix on the DCFC efficiency are investigated. A sensitivity analysis based on numerical simulations of the effects of cathode kinetic parameters and the anode specific surface area is also performed. Good agreement is obtained between numerical results and experimental data with an absolute average deviation of about 9%.

1. Introduction

Today, the world is over-reliant on oil and natural gas. Solid fuels, including carbon, provide promising alternative choices because of their wide availability [1]. In addition, developing new processes with improved energy conversion efficiency with the aim of reducing CO_2 emissions is important to alleviate global warming. Consequently, Direct Carbon Fuel Cells (DCFCs) have been receiving recently an increasing attention.

The Direct Carbon Fuel Cell (DCFC) differentiates from the Molten Carbonate Fuel Cell (MCFC) and the Solid Oxide Fuel Cell (SOFC) by using solid carbon as fuel [2]. It has the potential to convert the chemical energy of carbon directly into electricity without the need of gasification or the moving machinery associated with conventional electric generators.

One of significant advantages of this technology is the high energy density of solid carbon compared to that of alternative fuel sources such as hydrogen and methane both on a volumetric and mass density basis. Carbon fuels can be obtained from coal, cracking of hydrocarbons, or biochar issued from biomass pyrolysis [3].

DCFC systems show promising Open-Circuit Voltages (OCVs), but the current densities have not been enough to consider commercial applications. The difficulty in carbon oxidation in DCFCs is

* Corresponding author. Micro Electro Thermal Systems (METS), IPEIS, University of Sfax, BP1172, 3018 Sfax, Tunisia. Tel.: +216 98 954 415; fax: +216 74 246 347.
E-mail addresses: Kamel.Halouani@ipeis.rnu.tn, kamel_ipeis@yahoo.fr (K. Halouani).

0378-7753/$ – see front matter © 2013 Elsevier B.V. All rights reserved.
http://dx.doi.org/10.1016/j.jpowsour.2013.09.024

related to the carbon nature. The reactivity and fluidity of solid carbon are lower than those of gaseous fuels. Improving the anode kinetics is the key issue to achieve a high performance with DCFCs [3]. Thus, the use of a packed bed anode arrangement of carbon particles may contribute to the enhancement of the anodic kinetics performance by allowing better contact between carbon spheres [4].

The research on DCFC technology has received a great attention focusing on materials, structures, thermal management and reliability. In studying anodic electro-kinetics, researchers have focused on different aspects of the anode mechanisms of DCFC and the modeling approaches dealing with this problem are quite scarce. Few DCFC modeling study are available in literature.

Vutetakis and Skidmore [5] presented a complete polarization model of a DCFC with molten carbonate electrolyte. The electrochemical cell employed an anode of coal or carbon particles dispersed in a molten carbonate electrolyte at 500–800 °C. Results are presented for various forms and concentrations of carbon including open circuit potentials, current voltage curves and product gas evolution rates. The authors concluded that at 700 °C and above the measured potentials were in agreement with the theoretical values of the C/CO_2 redox couple.

Kornhauser [6] developed a DCFC electrochemical modeling based on fluidized bed configuration. He employed molten carbonate, with carbon fuel particles and oxidizer entrained and circulated through the electrodes. One of the major achievements of this work is to understand that the packed bed geometry is capable of producing large area per unit volume available for reaction. Large surface area when used for the chemical reaction produces high mass transfer rates. The effects of temperature and the carbon loading on the performance of the DCFC are also investigated.

Liu et al. [4] presented a developed ohmic polarization formulation for a packed anode structure of the DCFC. Results indicate that anode ohmic polarization is in the same magnitude as the highest loss affecting the DCFC performance (activation polarization) which is due to the low activity of carbon. The analytical model showed also that approximate total efficiency of the single cell is higher than 55% for low current density and 45–50% for high current density. Indeed, Liu et al. [7] simulated a highly efficient power system that combines a methane catalytic decomposition reactor (MCDR), DCFC and SOFC. The methane is decomposed to carbon and hydrogen. Carbon is used as fuel in the DCFC to generate power and pure CO_2. Hydrogen is used as fuel in the SOFC. Electrochemical modeling of the DCFC performance was developed in order to predict the polarizations, operating voltage, power output and exhaust temperature. This model presents an improvement to the model described later [4]. Results indicated that approximately 65% overall cell efficiency was achieved at a temperature range of 600–800 °C. The model permitted also to confirm that the DCFC is under anode activation polarization and ohmic polarization control.

Li et al. [8] developed an anode micro-structural model of carbon particle in molten carbonate configuration based of six step mechanisms assuming no rate determining step. Through this model, which accounts of the irreversibility of the anode process and supposing that the electrochemical oxidation of carbon takes place only at the edges of the graphene sheets, the performance of carbon black and graphite as fuel of DCFC was examined and showed an activation loss in the range of 0.024–0.28 V with a current density of 10–120 mA cm^{-2} at 700 to 900 °C. The developed analytical model is based on a modified anode reaction mechanism and a new method of rate calculation deduction. This helps to clarify and obtain the kinetic properties of the DCFC i.e. reaction rate, exchange current density and polarization losses.

Recently, Cooper et al. [9] criticized the structure-based kinetic model of the anode developed by Li et al. [8] and concluded that it should be combined with porous electrode theory to study the reaction distribution computational models. This model should be also tested using a well characterized carbon under well defined operating conditions to ensure the definition of a rate equation that should be estimated on the basis of reasonable determined values of the electrochemical factors and rate constants of each individual step of the studied mechanism.

Chen et al. [10] proposed a 1D macrohomogeneous model of carbon corrosion in a DCFC system by considering 4-electron carbon oxidation reaction, 2-electron CO oxidation reaction as well as the Boudouard reaction. Obtained results show that the active zone is located in the interface carbon/electrolyte and presents about 30% of the total height of the carbon particles bed. Simulation results confirm that the anodic DCFC performance is mainly controlled by the electrochemical oxidation of carbon.

Apart from the analytical cited models on DCFC electrochemistry, a recent numerical model had been developed by Alexander et al. [11]. They implemented an axisymmetric kinetic model of carbon bed in a solid carbon fuel cell using the finite element method to solve the coupled kinetic, gas mass conservation and gas transport equations inside the anode bed in order to induce the operational space of the fuel cell system. Numerical results revealed that the lower specific surface area and bulk density of the carbon offset by higher fuel reactivity in the dry gasification environment inside the anode. These authors concluded also that the cell performance increases with the onset of carbon conversion due to specific surface area increase. Then, it begins to decrease by around 50% fuel conversion as the loss of reactive material in the bed dominated its behavior.

Until now, mathematical modeling of DCFCs is still at the beginning stage and didn't yet account for the coupled electrodes electrochemistry with the heat and mass transport mechanisms. Therefore, understanding the interaction between these complex phenomena has such an explorative nature in this field.

In the literature, several concepts of DCFC have been presented by employing conventional electrolyte materials such as molten hydroxide [1], molten carbonate [12], and solid oxide [13]. The electrolyte is a critical material in the fuel cell. Indeed, the performance of the cell is dependent on the conductivity of the electrolyte materials. Also, the electrolyte has to be dense to prevent gas permeability to opposite sides and has a large area to minimize the bulk resistance. It should be an electronic insulator but a good ionic conductor. For state-of-the-art DCFC based solid oxide electrolyte such YSZ needs a temperature above 700 to 800 °C to ensure adequate ionic conductivity in order to guarantee sufficient power outputs.

In fact, a new research topic has been devoted to the development of new alternative electrolyte materials that operate at lower temperatures such as Samarium Doped Ceria (SDC). Ceria-carbonate composite electrolytes have attracted significant attention during the last decade for their application in Intermediate-Temperature Fuel Cells (IT-fuel cells).

Composite electrolytes usually show enhanced conductivity compared to the conventional solid electrolyte used in SOFCs and the molten carbonate electrolyte used in MCFCs, but the effects are not simply additive; rather they are synergistic which means that the global conductivity is significantly higher than in both of the constituent phases. The conductivity enhancement is suggested to be due to high ionic conductivity in the interface region between components [14,15]. In addition, composite electrolyte materials can be fabricated easily into a certain shape to support the fuel cell structure. These types of composite materials show a very promising performance when used as electrolyte in SOFCs.

The first DCFC apparatus based on ceria-composite electrolyte containing Li/Na carbonate eutectic and doped ceria phase is tested by Jia et al. [16]. A four-layer pellet cell is fabricated by a co-pressing and sintering technique. Commercial activated carbon powder is mixed with the composite electrolyte and is retained in the anode cavity above the anode current collector. With a suitable CO_2/O_2 ratio of the cathode gas, an operating temperature of 700 °C, a power density of 98 mW cm^{-2} at a current density of 200 mA cm^{-2} is achieved.

Elleuch et al. [17] investigated this type of composite electrolyte in a DCFC system fueled by slurry of graphite and molten carbonate. They demonstrated that the composite electrolyte is promising compared to the single constituent's electrolyte.

Although promising experimental results were achieved by our research group [17,18], design and operating parameters need to be optimized for maximum performance, so that a proper assessment can be made for possible future DCFC technology development. For that, a thought on mathematical modeling and computational simulations is recommended in order to predict how fuel cell performance is affected by the variation of operating conditions and geometrical parameters. Such model should be simple, computationally fast and able to capture reliably the DCFC behavior.

The purpose of this work, and hence its contribution, is to develop a preliminary mathematical model of a Lab-scale DCFC system in order to build a numerical tool enabling the numerical prediction of heat and mass transport phenomena effect on the electrochemistry of the DCFC and the assessment of the DCFC design optimization for a wide range of parameters.

This model takes into account of the electrochemical, mass and heat transfer phenomena in all regions of the cell simultaneously and permits to describe the temperature and species concentrations profiles all over the regions of the fuel cell. Parametric study is then performed to predict the effect of key operating parameters such as temperature, inlet gas flow velocity, electrolyte matrix porosity and anodic specific surface area on the DCFC performance. The model results are also specifically validated experimentally in *Tianjin Key Laboratory of Applied Catalysis Science and Technology, China* by using an actual state-of the-art DCFC system.

2. Experimental

2.1. Cell fabrication

Samarium Doped Ceria ($Ce_{0.8}Sm_{0.2}O_{1.9}$) sample was synthesized *via* oxalate co-precipitation process. The SDC precursor is sintered at 700 °C for 2 h to form the pale yellow SDC powder ($Ce_{0.8}Sm_{0.2}O_{1.9}$) [16,17]. Then, a binary carbonate eutectic powder, i.e. Li_2CO_3/Na_2CO_3 in a mole ratio of 2:1, was prepared by a process of sequential ball milling for 2 h, co-sintering at 700 °C for 2 h and grinding. Composite ceria-carbonate electrolyte material was obtained through mixing the last two powders (carbonate powder and SDC powder) in a weight ratio of 3:7 by ball milling for 2 h. The composite cathode powder, which consists of 30 wt% the composite electrolyte and 70 wt% the Lithiated Nickel Oxide ($Li_xNi_{1-x}O$) powders, was also prepared through 2 h ball mill mixing and sintering at 700 °C for 2 h. The cathode has a porous nature which facilitates reactant distribution across the reaction sites [19]. It includes some sites rich on nickel. The main role is to accelerate the electrochemical reaction occurrence. More details the reaction mechanisms are available in Ref. [20].

The two-layer DCFC was fabricated by dry-powder-pressing technique beginning by loading the composite electrolyte followed by the composite cathode powder with the aid of a 60 mesh sieve. The pressed cell size was 20 mm in diameter with the electrode surface area of 1 cm^2 and 1.4 mm in thickness which consists approximately on 0.8 mm thick composite electrolyte, and 0.6 mm thick composite cathode (Fig. 1).

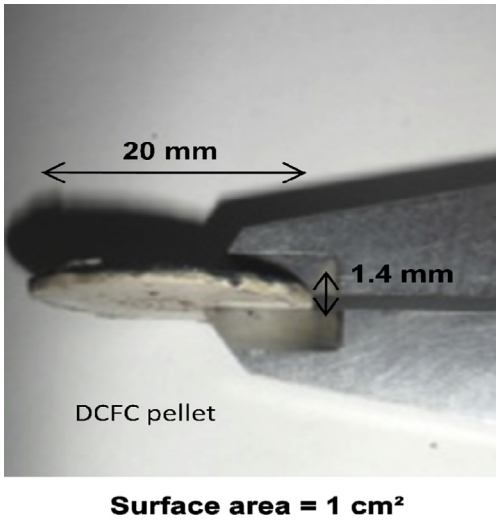

Fig. 1. Real design of the electrolyte/cathode pellet used for the DCFC performance measurement.

Slurry of anode material was prepared by adding molten carbonate electrolyte powders (Li_2CO_3/Na_2CO_3 in a mole ratio of 2:1) into graphite carbon particles. Ball-milled the mixture at 1000 rpm for 2 h, then the powder-like electrolytic material would be ready. The mass ratio of electrolyte to carbon materials was chosen to be 1:9 wt%. The carbon particles (graphite) forming the packed bed serve both as fuel and as electrode. The anode and cathode current collectors were made of silver ring. The two-layers DCFC was tested in a stainless steel apparatus sealed gas tight.

2.2. Experimental setup and testing procedures

The prepared DCFC pellet shown in Fig. 1 was placed in the center of a tubular electric furnace. A thermocouple (type K) was attached to measure the operating temperature of the cell. The cell was heated to its operating temperature at 5 °C min^{-1}. Nitrogen was employed as anode protective gas and a mixture of O_2 and CO_2 was used as cathode gas [17].

Once the required operating temperature was reached, *I–V* curves were collected by a VersaSTAT3 Electrochemical System using VersaStudio software for automatic data collection based on the linear sweep voltammetry method (LSV) at scan rate of 1 mV s^{-1}.

3. Mathematical model formulation

Fig. 2 schematically demonstrates the 2-D physical domain of the DCFC divided into four sub-domains: the anode, the composite electrolyte, the composite cathode and the cathode gas channel. The cell size was 1.4 mm in thickness which consists of a 0.8 mm thick composite electrolyte, and 0.6 mm thick composite cathode. The anode thickness was about 1 mm whereas the cathode gas channel is 0.8 mm thick. The cell is continuously supplied with reactants. On the cathode side, O_2 and CO_2 diffuse from the cathode gas channel (bulk phase) to the cathode reaction site through the porous structure. Within the interface cathode/composite electrolyte, oxygen can reacts alone and is converted to oxygen ions (O^{2-}) by consuming electrons according to possible Eq. (1), or when reacting with carbon dioxide, it is respectively converted to carbonate ions (CO_3^{2-}) according to Eq. (2).

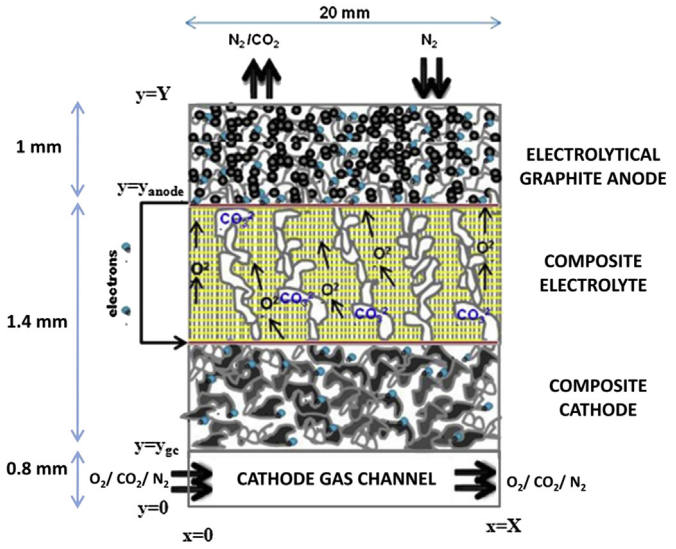

Fig. 2. The computational domain of the simulated DCFC geometry.

Both oxygen and carbonate ions could be transported through the dense layer of ceria-carbonate electrolyte to the anodic reaction site. The bed is supposed to be composed of several slabs of spherical carbon particles wetted with molten salts. Each particle is assumed to act as a rigid sphere and packed with a simple hexagonal pattern [4] (Fig. 3). Within the anode packed bed, carbon reacts with both oxygen and carbonate ions currying the electric current and releasing CO_2 according to Eqs. (3) and (4).

Cathode half cell reaction:

$$O_2 + 4e^- \rightarrow 2O^{2-} \quad (1)$$

$$O_2 + 2CO_2 + 4e^- \rightarrow 2CO_3^{2-} \quad (2)$$

Anode half cell reaction:

$$C + 2O^{2-} \rightarrow CO_2 + 4e^- \quad (3)$$

$$C + 2CO_3^{2-} \rightarrow 3CO_2 + 4e^- \quad (4)$$

Overall cell reaction:

$$C + O_2 \rightarrow CO_2 \quad (5)$$

Without losing the generic physical characteristics, every numerical simulation is conceived and developed based on a set of assumptions motivated by a lack of experimentally evaluated physical parameters. Likewise, in this model we assume that carbonate ions CO_3^{2-} predominates O^{2-} ions conduction on the ceria-carbonate composite electrolyte. This assumption is made according to the OCV-time and temperature curve which indicates the increase of the OCV just after the melting of the carbonate phase [21]. So, Eqs. (2) and (4) are adopted here as cathode and anode reaction respectively.

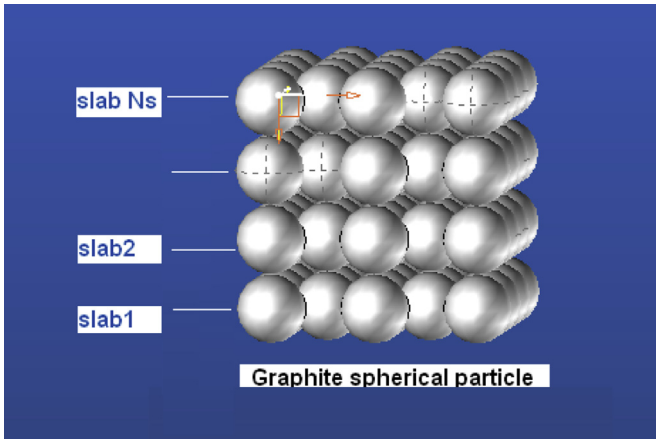

Fig. 3. Schematic drawing of the packed bed anode structure.

As the cell generates more current, its electric potential decreases due to the irreversible effects, i.e. the activation overpotentials caused by the electrochemical reaction energy barriers, the ohmic overpotentials caused by the electric resistance of the cell components and the concentration overpotentials caused by mass transfer limitations.

3.1. Governing equations

There are different global methodologies for modeling fuel cells. The easiest division to make is between macroscopic and microscopic models. The microscopic model seeks to model transport on an individual pore level, whereas the macroscopic ones are continuum and average over this level. Although the microscopic models may provide more realistic conditions and factors, they require a lot more knowledge of the microstructure and are much more expensive in terms of computation time. Macroscopic models are more common for fuel cells, although some microscopic details should be considered. In the macroscopic modeling approach, the exact geometric details of the modeling domain are neglected. Instead, the domain is treated as a randomly arranged porous structure that can be described by a small number of variables such as the porosity and surface area per unit volume. Furthermore, transport properties within the domain are averaged over the electrode volume. Thus, all variables are defined at all positions within the domain. Averaging is performed over a region that is small compared to the size of the electrode but large compared to the microstructure [22].

The macroscopic model is able to simulate a large-area cell which has high gas and carbon utilization and non uniform temperature distribution [23]. In fact, this paper focuses in developing a two dimensional macroscopic numerical model based on the single domain approach. For all regions of the computational domain (Fig. 2) of the fuel cell, the continuity, momentum, energy, and species transfer equations are written in the same form. However, the diffusion, convection, and source terms will vary depending on the local properties of the regions (eg. cathode gas channel, composite cathode, composite electrolyte, and graphitic anode).

The model is developed using the Cartesian coordinates. The pellet thickness is considered as *y*-direction and the pellet diameter as *x*-direction. The cell surface area is equal to 1 cm^2 for the both physical model and experimental pellet.

The model mathematical formulation assumes:

- Steady state
- Compressible and laminar flow

- Isotropic and homogeneous regions
- In the present model, the graphitic anode bed thickness is assumed to be constant (1 mm). This assumption is made on the basis of our experimental observation indicating a quasi-stationary slow drift of the graphite bed during the cell discharging tests. In fact, the experimental record of the *I–V* curve at a working temperature took only 2 min when graphite bed drift velocity is estimated to about 10^{-5} mm s^{-1} (very slow). The remaining anode bed thickness is always found higher than 1 mm thick.
- CO_2 is present in the entire computational domain except in the electrolyte. In fact, based on previous results in the literature [4,12], the concentration polarization in both electrodes caused by slow diffusion, solution/dissolution of reactants and products (O_2 and CO_2) into and out of the electrolyte, is neglected. For that, we fixed a very low permeability (10^{-30} m^2) for the composite electrolyte domain.
- Local thermal equilibrium between solid structure and fluid phase in the porous medium and hence one equation with effective heat conductivity can describe the heat transfer process.

By using these assumptions, the DCFC mathematical model is reduced to the following transport equations for the entire domain with variable diffusion and source terms which will be described below for each sub-domain:

■ Conservation of mass

$$\frac{\partial(\varepsilon\rho u)}{\partial x}+\frac{\partial(\varepsilon\rho v)}{\partial y} = \Phi_{CO_{2,a}} + \Phi_{O_2} + \Phi_{CO_{é,c}} \tag{6}$$

■ Conservation of momentum

$$\frac{\partial(\varepsilon\rho uu)}{\partial x}+\frac{\partial(\varepsilon\rho uv)}{\partial y} = -\frac{\partial P}{\partial x}+\frac{\partial}{\partial x}\left(\mu\frac{\partial(\varepsilon u)}{\partial x}\right)+\frac{\partial}{\partial y}\left(\mu\frac{\partial(\varepsilon u)}{\partial y}\right)-\frac{\varepsilon\mu}{K}u \tag{7}$$

$$\frac{\partial(\varepsilon\rho uv)}{\partial x}+\frac{\partial(\varepsilon\rho vv)}{\partial y} = -\frac{\partial P}{\partial y}+\frac{\partial}{\partial x}\left(\mu\frac{\partial(\varepsilon v)}{\partial x}\right)+\frac{\partial}{\partial y}\left(\mu\frac{\partial(\varepsilon v)}{\partial y}\right)-\frac{\varepsilon\mu}{K}v \tag{8}$$

■ Conservation of gaseous species

$$\frac{\partial}{\partial x}(\varepsilon C_i u)+\frac{\partial}{\partial y}(\varepsilon C_i v) = \frac{\partial}{\partial x}\left(D_{i,\mathrm{mix}}\frac{\partial C_i}{\partial x}\right)+\frac{\partial}{\partial y}\left(D_{i,mix}\frac{\partial C_i}{\partial y}\right) \quad \text{where } i = O_2,\ CO_2,\ N_2 \tag{9}$$

■ Conservation of energy

$$\frac{\partial(\varepsilon\rho C_p Tu)}{\partial x}+\frac{\partial(\varepsilon\rho C_p Tv)}{\partial y} = \frac{\partial}{\partial x}\left(\lambda\frac{\partial T}{\partial x}\right)+\frac{\partial}{\partial y}\left(\lambda\frac{\partial T}{\partial y}\right)+\Phi_{\mathrm{rev}}+\Phi_{\mathrm{act}}+\Phi_{\mathrm{ohm}}+\Phi_{\mathrm{ohm,elec}} \tag{10}$$

■ Conservation of charge

$$\frac{\partial}{\partial x}\left(\sigma\frac{\partial\varphi}{\partial x}\right)+\frac{\partial}{\partial y}\left(\sigma\frac{\partial\varphi}{\partial y}\right)+\Phi_\varphi = 0 \tag{11}$$

3.1.1. Cathode gas channel

In the cathode gas channel, the continuity Eq. (6) has no source terms in this region since there are no chemical reactions occurring. The momentum equations (Eqs. (7) and (8)) doesn't include the darcyan term since the cathode gas channel is not a porous medium. The source terms for the mass, energy and potential equations Eqs. (9)–(11) are also nil in this region of the computational domain.

The properties of the gaseous mixture in this region of the computational domain are calculated by taking into account the different species present locally. The mixture density (ρ), viscosity (μ) and mass diffusion ($D_{i,\mathrm{mix}}$) are respectively given by Ref. [24]:

$$\rho = \sum_i M_i C_i \tag{12}$$

$$\mu = \sum_i \frac{\rho_i}{\rho}\mu_i = \sum_i \frac{M_i C_i}{\rho}\mu_i \tag{13}$$

Where ρ_i is the density, μ_i is the viscosity, M_i the molar mass and C_i is the concentrations of the gaseous species *i*.

$$D_{i,\mathrm{mix}} = \frac{1-y_i}{\sum_{j\neq i} y_j/D_{ij}} \tag{14}$$

Where y_i is the molar fraction of species *i*, given by:

$$y_i = C_i/\sum_j C_j \tag{15}$$

The diffusion coefficient in Eq. (14) is based on the Stefan–Maxwell equations [24]. The binary diffusion coefficient D_{ij} for two species *i* and *j* for the local temperature and pressure is scaled as given in Eq. (16) [25]:

$$D_{ij} = D_{ij}^{\circ}\left(T^0, P^0\right)\left(P^0/P\right)\left(T/T^0\right)^{1.81} \tag{16}$$

The specific heat and thermal conductivity of the fluid mixture are given by Ref. [26]:

$$C_\mathrm{p} = \sum_i \frac{(C_i C_{\mathrm{p},i})/M_i}{\sum C_i},\quad i = O_2, CO_2, N_2 \tag{17}$$

$$\lambda = \sum_i y_i\lambda_i = \sum_i \frac{C_i}{\sum_j C_j}\lambda_i \tag{18}$$

Where the species properties $C_{\mathrm{p},i}$, λ_i and μ_i are given as a function of temperature [26].

3.1.2. Composite cathode

As mentioned earlier, the cathode is made of a porous composite material (Lithiated NiO-composite electrolyte) allowing convective and diffusive migration of the various species. The continuity equation Eq. (6) includes mass source term due to the occurrence of the cathode electrochemical reaction.

The source terms for oxygen and carbon dioxide species, Eqs. (19) and (20), account for the gas consumption *via* the half cathodic reaction.

Oxygen consumption:

$$\Phi_{O_2} = -j_c/(4F) \tag{19}$$

Carbon dioxide consumption in the cathode:

$$\Phi_{CO_2,c} = -j_c/(2F) \tag{20}$$

Chemical reactions, including electrochemical reactions, involve energy barriers which must be overcome by the reacting species. This energy barrier is called the activation energy and results in activation or charge-transfer polarization, which is due to the transfer of charges between the electronic and the ionic conductors. Activation polarization and the cathode local current density per unit volume (j_c) is normally expressed by the well known Butler–Volmer equation (Eq. (21)) as follows [27]:

$$j_c = a\_c \cdot j_{0c}\left[\exp(\alpha_c \eta_{act,c}(n_e F)/RT) - \exp(-(1-\alpha_c)\eta_{act,c}(n_e F)/RT)\right] \tag{21}$$

α_c is the transfer coefficient considered to be the fraction of the change in polarization that leads to a change in the cathodic reaction rate constant [27–30]. Meanwhile, the used cathode charge transfer coefficient (α_c) values in the present model are between 0.75 and 0.25 dependently on the applied potential (V_{cell}). The variation of the cathodic charge transfer coefficient is proposed due to the possible non uniform current or potential distributions in porous composite cathode structure which may be due to the presence of semiconducting layers at the cathode/electrolyte boundary. The heterogeneity of the composite cathode is seen clearly in the SEM micrographs [17] reflecting a random mixture of pore diameters and lengths resulting in a difference in the conductivity from one region to the other. The value of α_c less than 0.5 are seen also for the oxygen reduction reaction through a composite cathode (LSM–YSZ) in SOFC systems at high overpotentials [28–30].

The cathode active surface area (a_c) is also known as the specific reactive surface area ($m^2\ m^{-3}$). j_{0c} is the exchange current density of the cathode. It is detailed in Eq. (22) based on the peroxide mechanisms [4].

$$j_{0c} = j^0_{0\cdot c} P^{r_1}_{CO_2,c} P^{r_2}_{O_2} \tag{22}$$

The momentum Eqs. (7) and (8) are similar to those developed in the cathode gas channel, but contain an additional source term which is based on the Darcy law traducing the pressure drop caused by frictional drag in the porous cathode. This term is function of the medium permeability ($K_{cathode}$). The permeability given by Eq. (23) is defined as a function of the porosity ($\varepsilon_{cathode}$) and the pore diameter (D_p) of the porous cathode medium [31].

$$K_{cathode} = \left(D_p^2 \varepsilon^3_{cathode}\right) \Big/ \left(150(1-\varepsilon_{cathode})^2\right) \tag{23}$$

The pore diameter is normally between 8 μm and 12 μm for MCFC electrodes. Thus, the permeability is estimated to be around $1.9\cdot10^{-12}\ m^2$ [32].

The species conservation Eq. (9) and the energy equation Eq. (10) keep the same form as those given in the cathode gas channel compartment but with up-scaled variables (velocities and concentrations) and corrected fluid property (diffusion coefficient) to account for the porous domain.

Where $D_{i,mix,eff}$ is the effective mixture diffusivity coefficient taking account of the solid phase fluid presence and given by Eq. (24).

$$D_{i,mix,eff} = D_{i,mix}\varepsilon^{1.5}_{cathode} \tag{24}$$

It is a function of the mixture diffusion of the gaseous species in all regions of the computational domain which is calculated by taking into account the different species present locally Eq. (25).

$$D_{i,mix} = (1-y_i)/\sum_{j\neq i} y_j/D_{ij} \tag{25}$$

The energy equation is expressed by Eq. (10) and contains source terms for reversible heat Eq. (26), heat produced *via* activation losses Eq. (27), and ohmic heat resistance generated due to the irreversible resistance (material resistance) to current flow Eq. (28).

$$\Phi_{rev,c} = j_c(T\Delta S_{cathode}/4F) \tag{26}$$

$$\Phi_{act,c} = j_c \cdot \eta_{act,c} \tag{27}$$

$$\Phi_{ohm,c} = j_c^2/\sigma_{cat} \tag{28}$$

For the reversible heat source term, the entropy change related to the half cathodic reaction is taken from the MCFC literature due to the same reaction occurring in the cathode electrode (Eq. (2)) [33].

The effective thermal conductivity of the porous cathode side is given by Eq. (29).

$$\lambda_{eff,cathode} = \varepsilon_{cathode}\lambda_f + (1-\varepsilon_{cathode})\lambda_s \tag{29}$$

Where λ_f is the thermal conductivity of the fluid mixture given by Eq. (18) and λ_s is the solid thermal conductivity of the composite cathode material.

The potential conservation equation Eq. (11) include a source term given by Eq. (30) representing the consumption of ions *via* the electrochemical reactions in the cathode side. It depends on the current density which is defined using the Butler–Volmer relation, Eq. (21).

$$\Phi_\varphi = 2F\Phi_{O_2} = j_c/2 \tag{30}$$

The mass and heat transfer balances depends on the cathodic reaction rate which is based on the value of the local electrical current density. It is evaluated by the microscopic approach based on the peroxide mechanism in order to describe the electrochemistry of the composite cathode [4,23,32].

3.1.3. Composite electrolyte

The electrolyte is a mixture of molten carbonate with SDC powder (30/70 wt% = $Li_2Na_2CO_3$/SDC) sandwiched between the two fuel cell electrodes. The SDC powder is usually used as a porous solid support matrix to impregnate the melting carbonates. It is capable of transferring ions from the cathode to the anode and it blocks the gaseous species transfer such as O_2, N_2, and CO_2. Therefore, the permeability for the Darcy term is set to be a very small number ($K = 10^{-30}\ m^2$) in order to inhibit the migration of the gas species due to pressure drop between the cathode and the anode of the DCFC. Since the approach chosen here is the single domain, the momentum equations are solved in the electrolyte and they result into negligible velocity across it.

Eqs. (10) and (11) describe respectively the energy conservation and the ionic transport in the electrolyte. The ionic source term in the electrolyte is nil since no chemical reaction is occurring.

The energy equation in the electrolyte is similar to the one developed in the cathode side, but account for the local thermal conductivity change, the electrolyte porosity and the ohmic heat dissipation due to the ionic resistance. The ohmic source term is given by equation Eq. (31).

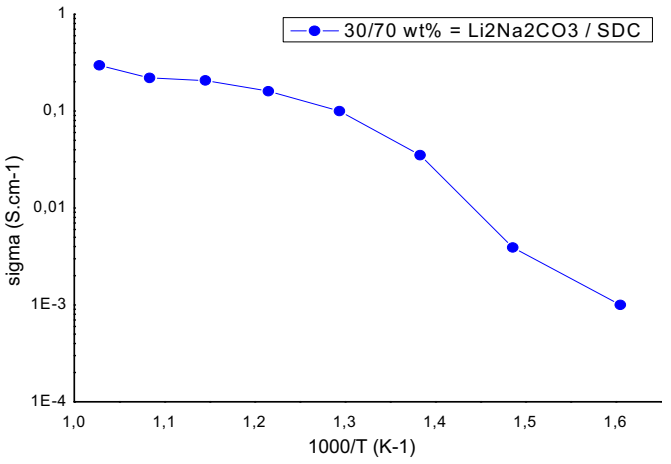

Fig. 4. Conductivity of the mixture of 67:33 mol% Li_2CO_3–Na_2CO_3/SDC in 3/7 weight ratio.

$$\phi_{ohm,elec} = j^2/\sigma_{elec} \tag{31}$$

The average direct carbon fuel cell current density is calculated using the local ionic current through the electrolyte and is calculated using the ohm's law at the interface cathode/electrolyte:

$$\bar{j} = \frac{1}{X}\int_0^X \sigma_{elec}\frac{\partial\varphi}{\partial y}dx \tag{32}$$

The conductivity of the composite electrolyte is deduced from the EIS data and written as follows [34]:

$$\sigma_{elec} = A/T\exp(-E_a/RT) \tag{33}$$

Temperature dependence of the conductivity for the 30/70 wt % = $Li_2Na_2CO_3$/SDC powders is plotted in an Arrhenius relation as shown in Fig. 4.

The measured conductivity of the composite electrolyte is between 10^{-3} and 10^{-1} S cm^{-1} in the temperature range of 350–700 °C much higher than that of pure SDC. The activation energy (E_a) of the composite electrolyte is derived by plotting the log (σT) as function of (1000/T) using Arrhenius expression. The obtained activation energy is dependent of temperature range and is low in both ranges supporting the high ionic conduction and transportation of the used composite electrolyte (Table 1).

3.1.4. Anode

The anode consists of carbon particles (graphite) that serves both as fuel and as electrode. Some carbon particles that are in contact with the electrolyte forms a paste of carbon fuel granules in a molten salt. In this region of the cell, the carbon electro-oxidation reaction takes place generating heat.

The governing equations are similar to those developed in the cathode side. The continuity source term Eq. (34) is taken into account due to the production of CO_2 in the anode compartment.

$$\Phi_{CO_{2,a}} = 3j_a/(4F) \tag{34}$$

The energy equation depends on the ohmic resistance Eq. (35), reversible heat Eq. (36) and heat generated from the activation loss Eq. (37).

$$\Phi_{ohm,a} = j_a^2/\sigma_c \tag{35}$$

Table 1
Measured conductivity of 30/70 wt% = (67:33 mol% Li_2CO_3–Na_2CO_3/SDC).

Temperature region	Activation energy (E_a)		Pre-exponential factor (A)
(°C)	(KJ mol^{-1})	(eV)	(S cm^{-1} K)
350–500	12.49	0.13	$9.79E^3$
500–700	38.6	0.4	$1.12E^7$

$$\Phi_{rev,a} = j_a(3T\Delta S_{anode}/4F) \tag{36}$$

$$\Phi_{act,a} = j_a \cdot \eta_{act,a} \tag{37}$$

The reversible heat source term in the reaction sites of the electrolytic graphite bed is dependent on the entropy change associated with the DCFC anodic reaction. This term cannot be directly calculated by thermodynamic correlations, because they involve the entropy associated to the ionic and electronic phase [35]. Certain authors tried to determine one of the entropy changes experimentally and to calculate the second as the difference between the entropy associated to the overall reaction (Eq. (5)) and the known entropy (in this case, the cathodic reaction entropy $\Delta S_{cathode}$). For the DCFC based molten carbonate electrolyte, the same cathodic reaction is employed. So, a literature research leads to the value of $\Delta S_{cathode} = -216.2$ J mol^{-1} K^{-1} [33]. The overall reaction entropy change of the DCFC system is about $\Delta S_{overall} = 1.6$ J mol^{-1} K^{-1} at ambient temperature. In fact, after taking into account of the stoichiometric coefficient we can notice that the entropy change of the anodic reaction within the DCFC is around $\Delta S_{anode} = 217.323$ J mol^{-1} K^{-1}.

The dissipation of heat in the DCFC is governed not only by electrochemical losses but also by reversible losses. Most of the reversible heat is dissipated in the cathode side. On the other hand, anode reaction has a positive entropy change leading to the conversion of heat into power.

The potential conservation equation Eq. (11) include a source term given by Eq. (38) representing the production of ions *via* the electrochemical reactions in the packed bed anode.

$$\Phi_\varphi = (2F/3)\Phi_{CO_2,a} \tag{38}$$

It is dependent on current density which is defined using the Butler–Volmer relation, Eq. (39).

$$j_a = a\_a \cdot j_{0a}\left[\exp(\alpha_a\eta_{act,a}(n_eF)/RT) - \exp(-(1-\alpha_a)\eta_{act,a}(n_eF)/RT)\right] \tag{39}$$

The activation loss is dependent on charge transfer coefficients (α_a) and on the anode active surface area (a_a). The used anodic charge transfer coefficient (α_a) was 0.75.

The anode exchange current density (j_{0a}) is related to the charge transfer resistance R_{ct} (Eq. (40)) and is given by Eq. (41) [4].

$$R_{ct} = 30.79 + 1.48\exp(T/28.58) \tag{40}$$

$$j_{0a} = RT/4FR_{ct} \tag{41}$$

One of the objectives of the present work, unlike previous studies, is to provide all required model input parameters to help scientists to have a better understanding of the model formulations. Hence, Tables 2 and 3 exhibit all physical and thermal, kinetic properties of the materials involved in the mathematical formulation.

Table 2
Operating conditions [17].

Description	Value
Anode inlet pressure (atm)	1
Cathode inlet pressure (atm)	1
Fuel cell temperature (K)	973
Length of the DCFC (m)	$1E^{-2}$
Width of the DCFC (m)	$1E^{-2}$
Carbon dioxide inlet flux (ml min^{-1})	120
Oxygen inlet flux (ml min^{-1})	60
Cathode inlet flow velocity (m s^{-1})	0.31
Cathode gas channel thickness (m)	$1E^{-3}$
Cathode thickness (m)	$0.6E^{-3}$
Electrolyte thickness (m)	$0.8E^{-3}$
Anode thickness (m)	$1E^{-3}$

3.1.5. Boundary conditions

The applied boundary conditions are as follows:

x-direction

- For the cathode inlet ($x = 0, 0 \le y \le y_{gc}$), a parabolic profile for u with average cathode gas velocity $\overline{u_c}$ is specified. The gaseous species flow the cathode gas channel only following the x-direction. In the inlet boundary of the cathode gas channel where only O_2, N_2 and CO_2 are flowing, there is no ion flow. The temperature of the gaseous species in the inlet of the cathode is imposed as T_c. These conditions are described by the following set of equations:

$$\begin{aligned} &v = 0 \\ &C_{CO_2,a} = 0,\ C_{CO_2,c} = C_1,\ C_{O_2} = C_2,\ C_{N_2} = C_3 \\ &\partial\varphi/\partial x = 0 \\ &T = T_c \end{aligned} \tag{42}$$

- For the cathode side, electrolyte and anode side inlet boundary conditions ie. at ($x = 0, y_{gc} \le y \le Y$), we suppose an insulated and impermeable boundary. Also no ion flow is present in this inlet boundary:

$$\begin{aligned} &u = v = 0 \\ &\partial T/\partial x = 0,\ \partial C_i/\partial x = 0 \text{ and } \partial\varphi/\partial x = 0 \end{aligned} \tag{43}$$

- For the exhaust cathode gas channel boundary conditions at ($x = X, 0 \le y \le y_{gc}$), there are a fully developed flow with no ion flow:

$$\begin{aligned} &\partial u/\partial x = 0 \text{ and } \partial v/\partial x = 0 \\ &\partial T/\partial x = 0,\ \partial C_i/\partial x = 0 \text{ and } \partial\varphi/\partial x = 0 \end{aligned} \tag{44}$$

- For the exhaust boundary conditions of the anode side, electrolyte and cathode meaning at ($x = X, y_{gc} \le y \le Y$), we suppose the same boundary conditions for the inlet:

$$\begin{aligned} &u = v = 0 \\ &\partial T/\partial x = 0,\ \partial C_i/\partial x = 0 \text{ and } \partial\varphi/\partial x = 0 \end{aligned} \tag{45}$$

y-direction

- For the lower boundary conditions i.e. at the cathode gas channel, the following boundary conditions are applied showing the use of an impermeable and insulated boundary with no ion flow. For the use of the Butler–Volmer model, the electronic potential in the cathode is supposed nil:

$$\begin{aligned} &u = v = 0 \\ &\partial T/\partial y = 0,\ \partial C_i/\partial y = 0 \text{ and } \partial\varphi/\partial y = 0 \\ &\varphi_{e,c} = 0 \end{aligned} \tag{46}$$

Table 3
Parameters used in the simulations.

Symbol	Parameter	Value	References
P_{anode}	Anode inlet pressure (atm)	1	[4,18]
$P_{cathode}$	Cathode inlet pressure (atm)	1	[4,18]
T_c	Fuel cell inlet temperature (K)	973	[4,18]
V_{th}	Open circuit voltage (V)	1.02	[44]
Y	Length of the DCFC (m)	$1E^{-2}$	[4]
Z	Width of the DCFC (m)	$1E^{-2}$	[4]
$P_{CO_2,c}$	CO_2 partial pressure in the cathode inlet (atm)	0.333	[17]
P_{O_2}	Oxygen partial pressure in the cathode inlet (atm)	0.666	[17]
$P_{CO_2,a}$	Produced anodic CO_2 partial pressure (atm)	1 atm	–
α_a	Anode charge transfer coefficient	0.75	–
α_c	Cathode charge transfer coefficient	0.25–0.75	–
$\lambda_{s,Li_xNi_{1-x}O}$	Thermal conductivity of the lithiated NiO cathode (W m^{-1} K^{-1})	0.9	[32]
$\lambda_{s,SDC}$	Thermal conductivity of the SDC (W m^{-1} K^{-1})	1.2	[45]
$\varepsilon_{LiNiO_2\ Li_xNi_{1-x}O}$	Porosity of the lithiated NiO cathode	0.62	[32]
ε_{SDC}	Porosity of the SDC/carbonate composite electrolyte	0.3524	[46]
D_p	Pore diameter of the lithiated NiO cathode (μm)	8–12	[32]
$K_{cathode}$	Permeability of the cathode (m^2)	$1.6E^{-12}$	[32]
a_c	Specific area of the cathode (m^{-1})	$3E^5$	[32]
$j^0_{0\cdot c}$	Concentration-independent exchange current density (A m^{-2})	500	[4]
r_1	Power of CO_2 partial pressure	−1.25	[4]
r_2	Power of O_2 partial pressure	0.375	[4]
σ_{cat}	Conductivity of the lithiated NiO cathode (S m^{-1})	3800	[47]
$\lambda_{electrolyte}$	Thermal conductivity of the electrolyte (W m^{-1} K^{-1})	2	[32]
λ_{anode}	Thermal conductivity of the anode (W m^{-1} K^{-1})	8–12	–
ε_{anode}	Porosity of the packed bed anode	0.396	[4]
a_a	Specific area of the anode (m^{-1})	$6E^3$	[10]
σ_c	Conductivity of carbon particles (S m^{-1})	$1.6E^5$	[4]

- From the upper boundary conditions i.e. at the anode, we suppose that the CO_2 is realized following a fully developed flow. For the use of the Butler–Volmer model, the electronic potential in the anode is supposed as follow:

$$\begin{aligned} &\partial u/\partial y = 0 \text{ and } \partial v/\partial y = 0 \\ &\partial T/\partial y = 0 \text{ and } \partial\varphi/\partial y = 0 \\ &C_{CO_2,a} = C_4,\ C_{CO_2,c} = 0,\ C_{O_2} = 0,\ C_{N_2} = 0 \\ &\varphi_{e,a} = V_{th} - V_{cell} \end{aligned} \tag{47}$$

3.1.6. Numerical approach

The set of differential equations governing the DCFC model along with the boundary conditions given above are solved by using the Finite Volume Method based on the SIMPLE algorithm [36]. The equations are solved using a non uniform staggered grid. The number of grid points used in the x-direction and y-direction are 22 by 45 respectively. The mesh is considered to be fine enough to capture all the transport, chemical and electrochemical processes occurring in the cell especially in the complex cathode Three-Phase-Boundaries (TPB) and in the anode bed. Cell component

dimensions can be found in Table 2. The FORTRAN code in the present model uses the power law scheme based on the Peclet number for calculating the convective and the diffusive flux in each differential equation. In principle the model is developed for 3D problems. However, since only one mesh element is generated in the *z*-direction, it becomes 2D in this study.

There are generally two ways of solving for the electrochemical cell efficiency: either the operating current density is given and different potential losses are calculated or the cell potential is set and the current density delivered by the fuel cell is then calculated using Eq. (32). The latter is called voltage to current approach (VTC) which has been adopted in this study [32].

4. Results and discussions

4.1. Model validation

The model results are validated with the experimental results carried out for the design and operating conditions given in Table 2 and the simulation parameters given in Table 3.

The experimental measurements of the DCFC performance were performed at 700 °C using a cathode gas mixture of 120 ml min^{-1} CO_2 flux and 60 ml min^{-1} O_2 flux. The N_2 flux is used as gas carrier in the present model. The same electrode material, thickness are employed in the modeling. In addition, the adequate composite electrolyte conductivity was estimated using Electrochemical Impedance Spectroscopy (EIS) method due to the large variations observed for several Ceria-carbonate composite electrolyte samples.

As shown in Fig. 5, the modeling results are in good agreement with the experimental measurements over the entire current density range with an absolute average deviation (AAD) of about 9%. The consistency of these two curves by itself is a model-validation measure but it also predicts a modeling of the electrochemical, mass and heat transport on all the DCFC sub-domains. For the high current density range the present model gives accurate prediction of the real cell behavior (AAD within 3%) and at low current density range the AAD is within 15%. These errors may be due to the fact that the activation polarization is modeled using an exponential law (Butler–Volmer equation) whereas during the experiments a linear behavior at high voltage and low current densities is depicted. It seems like the linear ohmic losses is majoring the DCFC polarization curve over the activation and concentration losses. A detailed polarization analysis will be developed in the next section.

For the following discussions, the parameters given in Tables 1 and 2 are used as the default values and a parametric study will be performed.

4.2. Simulation results

Fig. 6 shows the different overpotential losses (η) affecting the performance of the fuel cell at 700 °C as function of the current density. The polarization curve of the DCFC seen in Fig. 5 seems to have a linear behavior. This is suggested to be related to the domination of the ohmic polarization [17]. Conversely, opposite behavior is observed in the simulated overpotentials shown in the same figure. At highest current densities (i.e., higher $V_{th} - V_{cell}$), the ohmic overpotential become constant and the increase in losses is solely due to the anodic and cathodic activation overpotentials which are directly related to the electrochemical reaction kinetics. At high cell voltage (V_{cell}), the dominant overpotential is the anodic activation polarization. As the cell voltage drops, the current produced by the DCFC increases, the cathodic activation polarization become more important. The cathode activation loss exhibits a linear function of cell voltage since the current density is a hyperbolic function of the cell voltage as indicated by Fig. 5. The combined effect of both electrode activation loss results to the linear polarization curve.

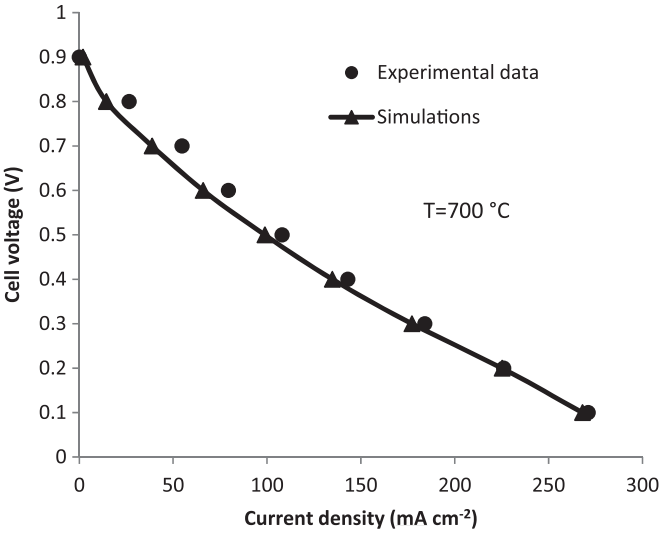

Fig. 5. Model validation curve using the experimental study of Elleuch et al. [17].

As it is shown the anode and cathode concentration overpotential doesn't affect the cell voltage curve at high cell voltage drop due to the fact that the anode is fueled by solid carbon which is always present during the cell test period. The issue was found to be in the porous composite cathode where the availability of gas mixture is always crucial which should neglect the drop off in the amount of current generation by the mass transfer limitation process.

The temperature distribution along the DCFC shown in Fig. 7 is simulated for $V_{cell} = 0.4$ V corresponding to the voltage giving the highest power density in this case. On the light of Fig. 7, it is evident that the temperature gradient in the *x*-direction is more significant compared to that in the *y*-direction due to the small dimensions in the *y*-direction compared to the *x*-direction. It can be seen that the heat of the gas is transferred along the *x*-direction *via* conduction and along the *y*-direction mainly by convection of gas flow.

In addition to the electrolytic ohmic loss, the major energy loss in the DCFC is due to electrode surfaces. There is a rapid reduction observed which has been attributed to the activation overpotentials of both electrode domains. Note that most of the heat dissipated in this case is due to the activation. Since activation magnitude is similar in the anode to the cathode (0.24 V) at this cell voltage, the heat is generated similarly within the anode and cathode regions.

The temperature in the cathode region is slightly lower than the anode due to the reversible heat which is converted into electrical power in the anode side by assuming a positive entropy change of this electrochemical reaction site ($\Delta S_{anode} > 0$).

In general the temperature variation (ΔT) from the inlet 973 K to the outlet 987.6 K seems to be around 15 °C which could be explained by the near zero entropy change of the single DCFC system.

Fig. 8 shows the carbon dioxide (CO_2) profile yield in the anode sub-domain of the DCFC. The obtained results show that the high carbon dioxide concentration value is present in the interface anode/electrolyte where the carbon anodic oxidation to carbon dioxide occurs. The concentration of CO_2 diffusing within the porous anode decreases slightly through the anode packed bed thickness. It is obvious that the upper boundary condition for

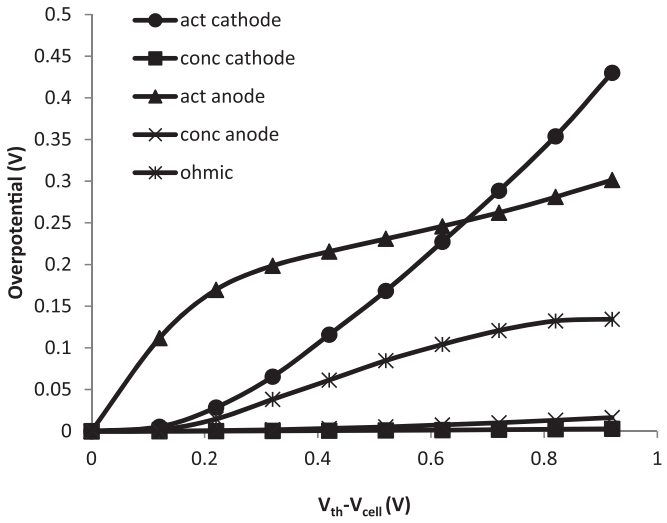

Fig. 6. DCFC potential losses at 700 °C.

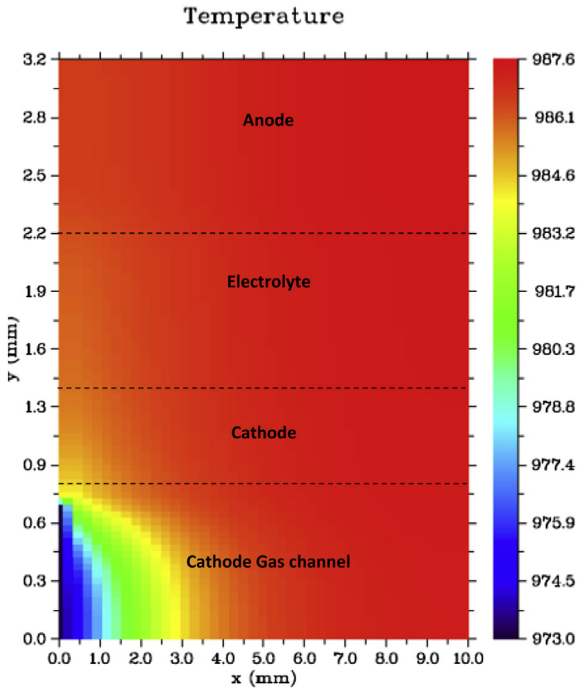

Fig. 7. Distribution of temperature in the DCFC (operating cell voltage V_{cell} = 0.4 V).

carbon dioxide concentration is set at atmospheric pressure and anodic fuel cell temperature to 13 mol m^{-3}.

Fig. 9 shows the oxygen concentration (O_2) profile in the cathode sub-domain. The oxygen concentration starts from the inlet value and decreases through the gas channel and the porous composite cathode media as it is consumed. The effect of the consumption of oxygen can be seen in the three phase boundary (TPB) of the cathode (the higher concentration gradient). This could be explained by the local cathode electrochemical reaction occurrence. It is also notable that the oxygen concentration gradient is significant in both directions due to the O_2 2D-diffusion and the continuous consumption in the reaction zone.

4.3. Parametric study

In this section, we propose to investigate the effect of some key parameters (temperature, anode specific surface area, cathode kinetics, cathode gas composition and composite electrolyte porosity) on the DCFC performance.

The validated model was used to perform in depth analyses to gain understanding of the activation, concentration and ohmic overpotentials of a DCFC under different operating conditions.

Fig. 10 shows the effect of temperature on DCFC performance. Typically, the operating temperature of the DCFC is above the melting temperature of the carbonate in the range of 600–700 °C. The modeling results predict well the experimental data dependently on the operating temperature. As the operating temperature increases, an improvement in the fuel cell performance is observed due to the fact that physico-electrochemical properties such as activation energies, binary species diffusivities and ionic conductivities are enhanced with the increase of temperature. This effect is clearly illustrated in Fig. 10 by the slope of the polarization curve that decreases from 364 μΩ m^{-2} at 873 K to 269 μΩ m^{-2} at 973 K more at higher temperatures.

The activation overpotential was found to decrease with increasing temperature. At a higher operating temperature, the electrodes became more reactive, and thus, the activation overpotential decreased and more current is generated. This is related to using the temperature dependent exchange current density in the anodic Butler–Volmer equation for evaluation of the activation overpotential.

As expected, it was found that the ohmic overpotential decreased drastically with increasing temperature from 0.1823 V at 873 K to 0.1343 at 973 K because the high ionic conductivity of the electrolyte was very sensitive to temperature. Therefore, in order to improve the performance of an intermediate temperature DCFC operating at 873–973 K, the electrolyte should have a high ionic conductivity, and the thickness should be kept smaller than 800 μm to reduce the ohmic overpotential.

It is well known that the DCFC performance depends greatly on the cathode oxygen gas concentration [16]. The result of the present model confirms this dependence as shown in Fig. 11 where three O_2 concentrations are tested. The DCFC performance is enhanced and the limiting current density increases when higher O_2 concentration is added to the cathode gas since more reacting gaseous species are reaching the TPB which affect the reaction rate and decreases the concentration overpotential. The DCFC seems to have a high limit operating cathode gas composition since the amelioration of performance between 2.060 mol m^{-3} and 4.015 mol m^{-3} are limited. Based on the present model results, the optimum cathode gas composition needed to achieve high performance of the composite electrolyte DCFC system is $CO_2/O_2 = 2/1$ mol%. These results agree well with those reported earlier by experiments [16].

Fig. 11 exhibits a multiplicity of current–voltage curve profile at different oxygen inlet concentration. For small oxygen concentrations (0.062 mol m^{-3}), a non-standard behavior was observed at a current density of about 100 mA cm^{-2} relative to the occurrence of a non-linear operating behavior. The I–V curve exhibits a branch with a negative differential resistance (NDR) which could be related to the nonlinear rate laws of the electrochemical reactions taking place at the electrodes or to the transport of charged and uncharged species within the various DCFC components which follows nonlinear kinetics laws, multi-driving force transport mechanisms and even two-phase flows [37].

The falling of the polarization curve at lower O_2 content is due to mass transfer limitation process which indicates that there is a minimal O_2 concentration to be used in cathode gas for better DCFC functioning ($C_{O_{2,lim}}$).

Indeed, the low oxygen concentration could affect the kinetic mechanisms (Eq. (22)) which exhibits a non-linear behavior and

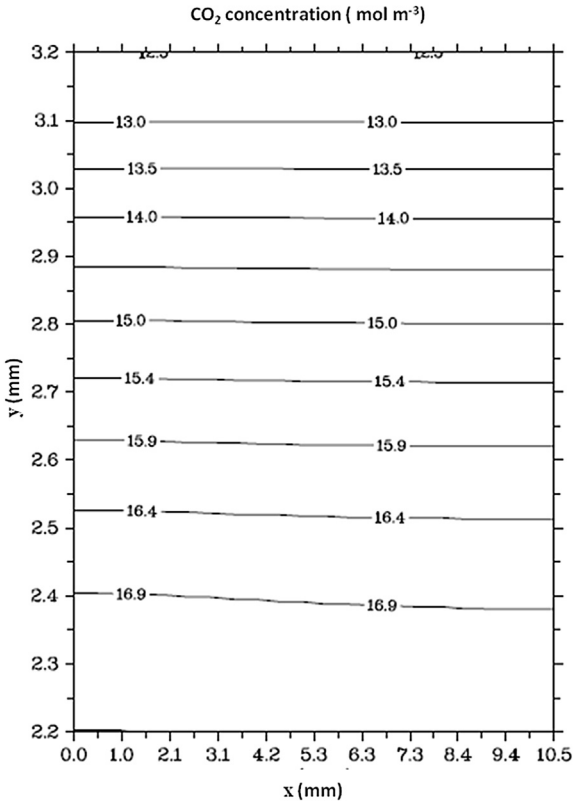

Fig. 8. Carbon dioxide concentration profile produced over the anode sub-domain (operating cell voltage $V_{cell} = 0.4$ V).

leads to this non-standard shape of the *I–V* curve. This observed non-standard behavior may be also related to the electrical conductivity of the electrolyte which depends strongly on the fuel cell's temperature. The heat released by the electrochemical reaction increases the cell temperature and hence the electrolyte conductivity which leads to a higher rate of migration of CO_3^{2-} ions to the anode side and a higher rate of carbon oxidation. For a given cell voltage, this leads to a higher cell current and to the generation of more heat. This positive feedback between ions migration and heat generation may cause this steady state multiplicity in the DCFC system. It seems that there is presence of a self-accelerating effect analogous to water formation in PEMFCs which is at the origin of the steady-state multiplicity including the hot spots in SOFCs and wet spots in PEMFCs [37,38].

The exchange current density is concentration dependent as discussed earlier. CO_2 concentration is raised to negative power of −1.25 and O_2 concentration is raised to a positive power of 0.375 as given by Eq. (22). Increasing the concentration of O_2 increases the local cathode current density and hence decreases the cathodic activation polarization as shown in Fig. 11. Prins-Jansen et al. [39,40] have performed impedance analysis and have concluded that the MCFC resistance rises with CO_2 concentration and decreases with a high O_2 concentration, which well agrees with the obtained modeling results.

The DCFC shares the same electrochemical cathode mechanism. Various mechanisms have been proposed for the cathode reaction in MCFC. The oxygen reduction mechanism under the MCFC cathode conditions has been described as several elemental reactions as follows [41]:

$$O_2, CO_2\,(g) \leftrightarrow O_2, CO_2\,(e) \tag{48}$$

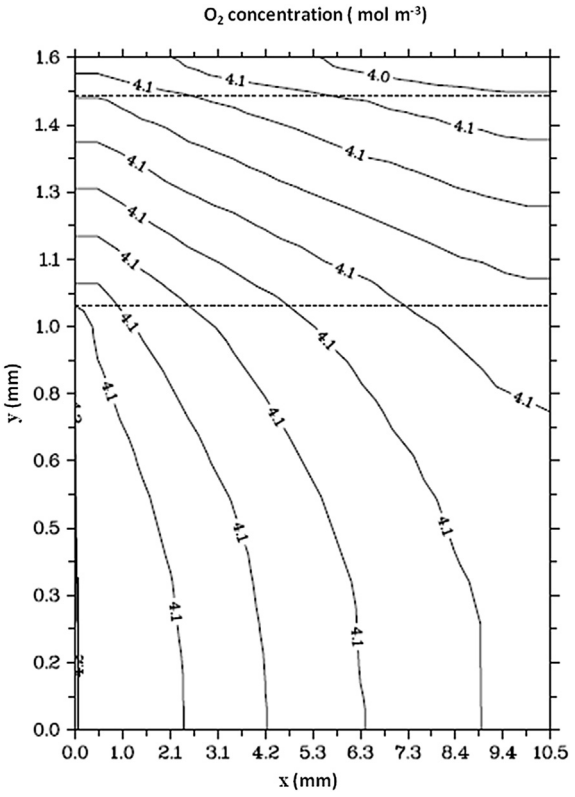

Fig. 9. Oxygen concentration profile over the cathode sub-domain (operating cell voltage $V_{cell} = 0.4$ V).

$$O_2 + 2CO_3^{2-} \leftrightarrow 2O_2^{2-} + 2CO_2(e) \tag{49}$$

$$O_2 + O_2^{2-} \leftrightarrow 2O^{2-} \tag{50}$$

$$O^{2-} + e^- \leftrightarrow O_2^{2-}(\text{superoxide RDS}) \tag{51}$$

$$O_2^{2-} + e^- \leftrightarrow O^{2-} + O^-(\text{peroxide RDS}) \tag{52}$$

$$O^- + e^- \leftrightarrow O^{2-} \tag{53}$$

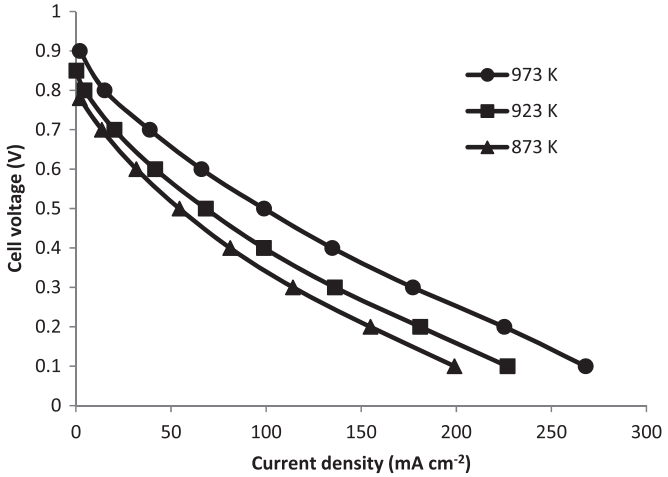

Fig. 10. Temperature effect on current density. a) ●— at 973 K, b) ■— at 932 K, c) ▲— at 873 K.

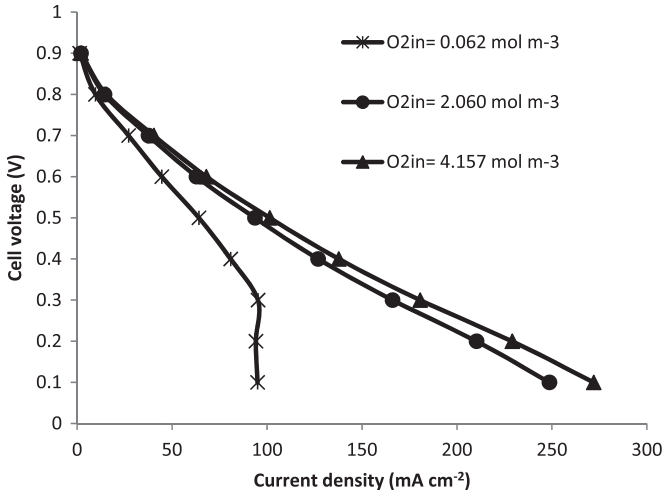

Fig. 11. Cathode gas composition effect on the DCFC performance. a) ⊣✳⊢ at $O_{2in} = 4.157$ mol m^{-3}, b) ⊣●⊢ at $O_{2in} = 2.060$ mol m^{-3}, c) ⊣▲⊢ at $O_{2in} = 0.062$ mol m^{-3}.

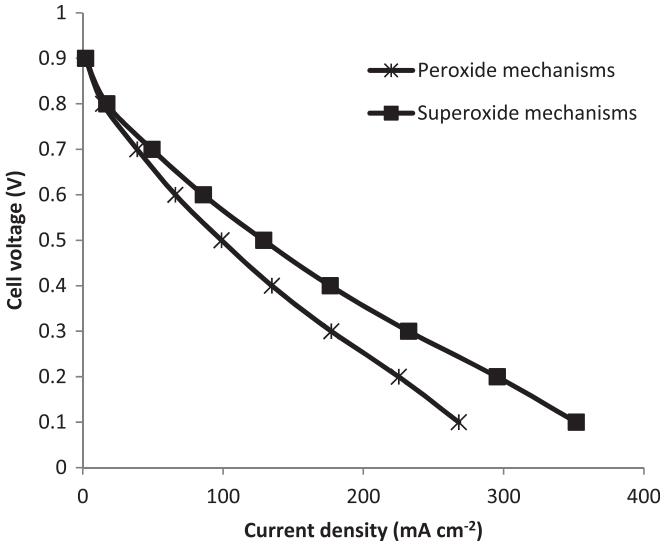

Fig. 12. Evaluation of the DCFC polarization curve between: a) ⊣✳⊢ the peroxide and b) ⊣■⊢ the superoxide model predictions.

$$O^{2-} + CO_2(e) \leftrightarrow CO_3^{2-} \quad (54)$$

It is composed of two slower reactions (Eqs. (51) and (52)) that limit the oxygen reduction rate. These reactions are the reduction of the peroxide ions and the reduction of the superoxide ions. Experimentally, if the oxygen reduction mechanism is limited by a superoxide or a peroxide reduction reaction, then one semicircular arc should be observed on the EIS spectra; if it is limited by a mixed peroxide–superoxide reduction mechanism with similar superoxide and peroxide reduction rates, there should be two semicircular arcs more or less superimposed [40]. The prediction capability of theses mechanisms is rarely discussed in literature. Therefore, the two most common reaction mechanisms, namely the peroxide [4] and the superoxide mechanisms [32] are employed and compared in Fig. 12. Both mechanisms have the same general form but vary by the exponents of the reaction orders in Eq. (22).

Obtained results reveal that the superoxide mechanism causes higher DCFC performance. This is explained by the tendency of the reaction rate (or volumetric current density) to increase with greater magnitude of the negative exponent of the CO_2 concentration ($r_1 = -0.75$) and larger magnitude of the positive value of O_2 concentration ($r_2 = 0.625$) in Eq. (22).

Moreover, numerical simulations indicate that at 700 °C, the peroxide mechanism is more predictive to the experimental analysis than the superoxide mechanisms. So, the cathode mechanism seems to be under peroxide mechanisms electrochemistry control.

Similar to electrolyte conductivity, the cathode electrochemical reduction rate vary significantly with different materials use. The state-of-art cathode material in MCFC is NiO with an exchange current density of 8.1 A m^{-2}. The tested composite cathode is made of lithiated NiO [17].

Fig. 13 presents the DCFC polarization curves for various cathode exchange current density values at 700 °C. As seen from the plot, varying j_{0c} has a significant effect on the polarization loss. As j_{0c} decreases the cathodic activation overpotential increases as a result of increased kinetic resistance. Consequently, the performance drops drastically to 69 mA cm^{-2} at lower exchange current density. Therefore, the development of scientific research on cathode materials properties enhancement needs to be more intensive.

As shown in Fig. 14, an increase in the anode specific area increases the DCFC performance at an operating temperature of 700 °C. The rise in the specific surface area enlarges the anodic reaction site and consequently permits an efficient wetting ability of carbon particle with molten carbonate. This leads to a faster carbon oxidation reaction. Thus, the energy barrier needed for the occurrence of the reaction named activation polarization is decreased resulting in improved cell efficiency.

This parameter varies dependently on the carbon fuel sample thus it is very important to describe the anodic active reaction sites. The activation polarization at $V_{th} - V_{cell} = 0.92$ V decreases from 0.43 V at 60 cm^{-1} to 0.23 V at 600 cm^{-1}. This is again consistent with the findings from Fig. 6 indicating that the anode activation polarization had the most significant contribution to the overall performance.

On the light of the obtained results, we can say that for improving the DCFC performance it is necessary to use a carbon with a high specific surface area to enhance its wet ability by the molten carbonate electrolyte.

The effect of the electrolyte porosity on the cell voltage curve is shown in Fig. 15. The use of low electrolyte porosity has a significant impact on fuel cell performance by reducing the overall current limit without showing the mass transfer limitation falling. Using different electrolyte matrix porosity, the mass diffusion limitation process does not appear in the DCFC polarization curve due to the fact that in DCFC concentration losses are negligible compared to the activation and ohmic losses. By increasing the electrolyte porosity, the diffusion of carbonate ions (CO_3^{2-}) to the anode reaction site becomes easier. So, the anodic reaction becomes more active and then reduces the anodic activation losses. At higher electrolyte porosity, the concentration overpotentials became clear. As can be seen in Fig. 15, the higher the electrolyte porosity the greater the power delivered by the DCFC. We can notice that the performance of the DCFC seems to be effectively improved by adjusting the microstructure of the composite electrolyte. This adjustment could be made through trying several preparation methods of the composite electrolyte including Sol–Gel process, Glycerine–Nitrate combustion process, carbonate co-precipitation or solid state reaction. The review of the influence of the above cited preparation method on the final composite electrolyte powder is reviewed by several authors [42,43].

The DCFC performances increases as the cathode inlet gas flow increases. Hence the polarization decreases with the rise in the gas flow velocity as shown in Fig. 16. The cell performance is enhanced by the using larger amount of reactant because more ionic

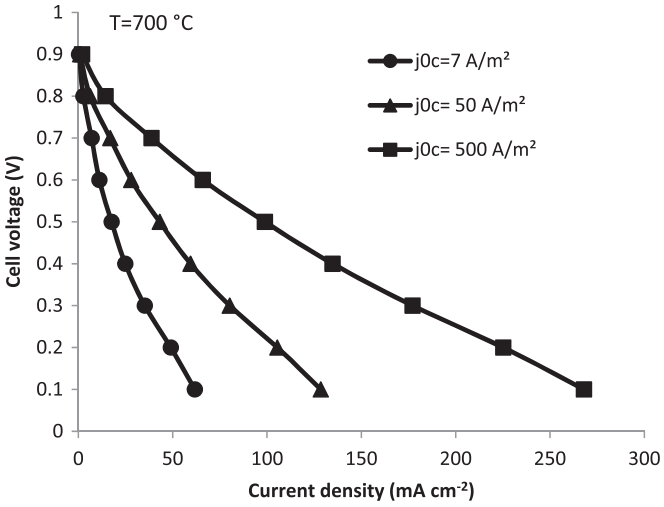

Fig. 13. Comparison of the DCFC performance for varying cathode independent temperature exchange current density. a) -●- at 7 A m^{-2}, b) -▲- at 50 A m^{-2}, c) -■- at 500 A m^{-2}.

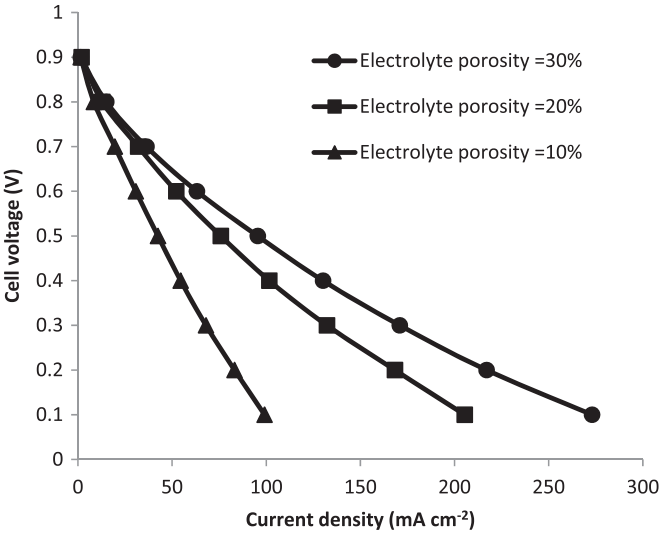

Fig. 15. Variation of the DCFC performance with the electrolyte matrix porosity. a) -●- at 30%, b) -■- at 20%, c) -▲- at 10%.

generation in the TPB can be reached *via* accelerated cathodic reduction and anodic carbon oxidation electrochemical reaction rates. The high velocity reduces the concentration gradient between bulk and superficial layer which decreases the concentration polarization effect.

5. Conclusion

In this study, a 2-D numerical model of a direct carbon fuel cell is developed to simulate the cell performance by taking into account of the electrochemical reaction mechanisms, mass and heat transfer and electrode materials characteristics and processes. This proposed model allows the prediction of the effect of the operating conditions (temperature, cathode kinetic, matrix porosity and anode specific area) on the DCFC performance. It permits also the investigation of temperature and species concentrations profiles within the DCFC based on composite electrolyte. Experimental validation of the DCFC performance fueled by a mixture of graphite and molten carbonate is also performed showing a good agreement with an absolute average deviation of about 9%. Results show that the linear tendency of the polarization curve is not solely related to the ohmic loss control but also it is a result of a combined effect of the anode and cathode activation loss. The temperature distribution through the DCFC computational domain varied by 15 °C among all the cell sub-domains due to the near zero entropy change. Comparison between the cathode kinetic mechanisms indicates that the peroxide mechanism predicts the DCFC polarization curve accurately. Results show that the high cathode inlet gas flow velocity is a key parameter accelerating the electrochemical reaction in the cathode TPB. Simulations are conducted to evaluate the effect of the anode specific surface area. It is found that increasing this parameter can enhance the cell performance. The produced current density is also significantly improved at a more porous electrolyte matrix. Further work is needed to improve the capabilities of the present model. In fact, we project to include effects of the non local thermal equilibrium within the porous media (between the solid and gaseous phase). This model will also be extended to simulate three-dimensional effects in order to capture geometrical phenomena effects.

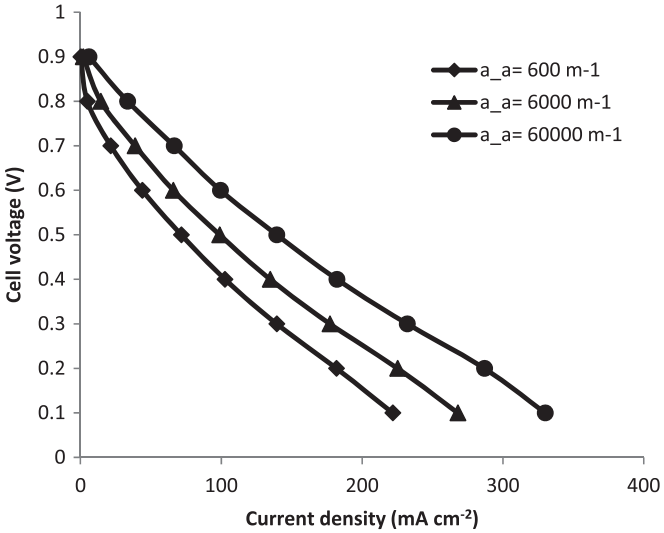

Fig. 14. Effect of the anode specific surface area on the DCFC performance. a) -◆- at 600 m^{-1}, b) -▲- at 6000 m^{-1}, c) -●- at 60,000 m^{-1}.

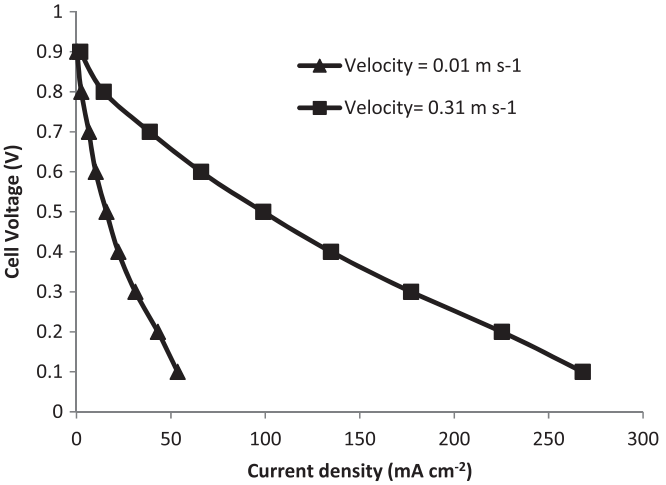

Fig. 16. Variation of the DCFC performance with the inlet gas flow velocity. a) -▲- at 0.01 m s^{-1}, b) -■- at 0.31 m s^{-1}.

References

[1] S. Zecevic, E.M. Patton, P. Parhami, Carbon 42 (2004) 1983–1993.
[2] M. Chen, Ch. Wang, X. Niu, S. Zhao, J. Tang, B. Zhu, Int. J. Hydrogen Energy 35 (2010) 2732–2736.
[3] Y. Nabae, K.D. Pointon, J.T.S. Irvine, J. Electrochem. Soc. 156 (2009) B716–B720.
[4] Q. Liu, Ye. Tian, Ch. Xia, L.T. Thompson, B. Liang, Y. Li, J. Power Sources 185 (2008) 1022–1029.
[5] D.G. Vutetakis, D.R. Skidmore, J. Electrochem. Soc. 134 (1987) 3027–3035.
[6] A. Kornhauser, R. Agarwal, Final Report, Virginia Polytechnic Institute and State University, Blacksburg, VA 24061-0238, 2004.
[7] Q. Liu, Y. Tian, H. Li, L. Jia, Ch. Xia, L.T. Thompson, Y. Li, J. Power Sources 195 (2010) 6539–6548.
[8] H. Li, Q. Liu, Y. Li, Electrochim. Acta 55 (2010) 1958–1965.
[9] J.F. Cooper, J.R. Selman, Int. J. Hydrogen Energy 37 (2012) 19319–19328.
[10] C.C. Chen, J.R. Selman, ECS Trans. 28 (2010) 31–43.
[11] B.R. Alexander, R.E. Mitchell, T.M. Gur, J. Electrochem. Soc. 159 (2012) B347–B354.
[12] W.H.A. Peelen, M. Olivry, S.F. Au, J.D. Fehribach, K. Hemmes, J. Appl. Electrochem. 30 (2000) 1389–1395.
[13] S. Li, A.C. Lee, R.E. Mitchell, T.M. Gur, Solid State Ionics 179 (2008) 1549–1552.
[14] J. Maier, Solid State Ionics 175 (2004) 7–12.
[15] H.L. Tuller, Solid State Ionics 131 (2000) 143–157.
[16] L. Jia, Y. Tian, Q. Liu, C. Xia, J. Yu, Z. Wang, Y. Zhao, Y. Li, J. Power Sources 195 (2010) 5581–5586.
[17] A. Elleuch, J. Yu, A. Boussetta, K. Halouani, Y. Li, Int. J. Hydrogen Energy 38 (2013) 8514–8523.
[18] A. Elleuch, A. Boussetta, K. Halouani, J. Electroanal. Chem. 668 (2012) 99–106.
[19] J.F. Cooper, in: S. Basu (Ed.), Recent Trends in Fuel Cell Science and Technology, Indian Institute of Technology Delhi, New Delhi-110 016, India, 2007, p. 257.
[20] Y. Izaki, Y. Mugikura, T. Watanabe, M. Kawase, J.R. Selman, J. Power Sources 75 (1998) 236–243.
[21] C. Xia, Y. Li, Y. Tian, Q. Liu, Y. Zhao, L. Jia, Y. Li, J. Power Sources 188 (2009) 156–162.
[22] A.Z. Weber, J. Newman, Chem. Rev. 104 (2004) 4679–4726.
[23] C.Y. Yuh, J.R. Selman, J. Electrochem. Soc. 139 (1992) 1373–1379.
[24] M. Sahraoui, Ch. Kharrat, K. Halouani, Int. J. Hydrogen Energy 34 (2009) 3091–3103.
[25] W.J. Massman, Atmos. Environ. 32 (1998) 1111–1127.
[26] B. Todd, J.B. Young, J. Power Sources 110 (2002) 186–200.
[27] T. Aloui, K. Halouani, Appl. Therm. Eng. 27 (2007) 731–737.
[28] Y. Zheng, R. Ran, Z. Shao, J. Phys. Chem. C 112 (2008) 18690–18700.
[29] A.C. Co, V.I. Birss, J. Phys. Chem. B 110 (2006) 11299–11309.
[30] J.N. Soderberg, A.C. Co, A.H.C. Sirk, V.I. Birss, J. Phys. Chem. B 110 (2006) 10401–10410.
[31] D.L. Giltrap, R. Mckibbin, G.R.G. Barnes, Sol. Energy 74 (2003) 85–91.
[32] M.Y. Ramandi, P. Berg, I. Dincer, J. Power Sources 218 (2012) 192–203.
[33] F. Yoshiba, Int. J. Energy Res. 28 (2004) 1361–1377.
[34] W. Liu, Y. Liu, B. Li, T.D. Sparks, X. Wei, W. Pan, Compos. Sci. Technol. 70 (2010) 181–185.
[35] R. Bove, S. Ubertini, Modeling Solid Oxide Fuel Cells: Methods, Procedures and Techniques, in: Fuel Cells and Hydrogen Energy, SPRINGER, 2008, p. 65.
[36] S.V. Patankar, Numerical Heat Transfer and Fluid Flow, Hemisphere Publishing Corp., Washington, DC, 1980, p. 210.
[37] R. Hancke-Rauschenbach, M. Mangold, K. Sundmacher, Rev. Chem. Eng. 27 (2011) 23–52.
[38] M. Bavarian, M. Soroush, Ind. Eng. Chem. Res. 49 (2010) 7922–7950.
[39] J.A. Prins-Jansen, J.D. Fehribach, K. Hemmes, J.H.W. de Wit, J. Electrochem. Soc. 143 (1996) 1617–1628.
[40] J.A. Prins-Jansen, K. Hemmes, J.H.W. de Wit, Electrochem. Acta 40 (1997) 3585–3600.
[41] F.J. Perez, D. Duday, M.P. Hierro, C. Gomez, M. Romero, M.T. Casais, J.A. Alonso, M.J. Martınez, L. Daza, J. Power Sources 86 (2000) 309–315.
[42] S.A. Muhammed Ali, A. Muchtara, N. Muhamada, A.B. Sulonga, in: IEEE Proc – First Conference on Clean Energy and Technology CET, 2011, pp. 394–399.
[43] C. Xia, Y. Li, Y. Tian, Q. Liua, Z. Wang, L. Jia, Y. Zhao, Y. Li, J. Power Sources 195 (2010) 3149–3154.
[44] D. Cao, Y. Sun, G. Wang, J. Power Sources 167 (2007) 250–257.
[45] R.V. Mangalaraja, S. Ananthakumar, M. Paulraj, H. Pesenti, M. López, C.P. Camurri, L.A. Barcos, R.E. Avila, J. Alloy. Compd. 510 (2012) 134–140.
[46] Y. Shilong, Y. Zhupeng, L. Chuanming, C. Xiaowei, Z. Yanwei, Mater. Lett. 92 (2013) 78–81.
[47] H.J. Choi, S.K. Ihm, T.H. Lim, S.A. Hong, J. Power Sources 61 (1996) 239–245.

Nomenclature

a_a: anode specific surface area (m^{-1})
a_c: cathode specific surface area (m^{-1})
C_i: concentration of species i (mol m^{-3})
Cp: specific heat at constant pressure (J mol^{-1} K^{-1})
D: diffusion coefficient (m^2 s^{-1})
D_p: pore diameter (m)
F: Faraday's constant (96,487 C mol^{-1})
j: current density (A m^{-2})
j_e: current density of the electrode e (a: anode, c: cathode) (A m^{-2})
j_{0c}: cathode exchange current density (A m^{-2})
$j^0_{0,c}$: concentration independent cathode exchange current density (A m^{-2})
K_i: permeability (m^2)
M_i: mass molar of species i (g mol^{-1})
n_e: electron number
n_i: molar number of species i
P: partial pressure (atm)
P_{anode}: anode inlet pressure (atm)
$P_{cathode}$: cathode inlet pressure (atm)
R: ideal gas constant (8.314 J mol K^{-1})
R_{ct}: charge transfer resistance (Ω m^2)
Φ_{O_2}: mass source term of oxygen (mol m^{-3} s^{-1})
$\Phi_{CO_{2,c}}$: mass source term of carbon dioxide consumed in the cathode (mol m^{-3} s^{-1})
$\Phi_{CO_{2,a}}$: mass source term of carbon dioxide produced in the anode (mol m^{-3} s^{-1})
Φ_{rev}: reversible heat source term (W m^{-3})
Φ_{act}: activation heat source term (W m^{-3})
$\Phi_{ohm,elec}$: ohmic heat source term in the electrolyte (W m^{-3})
$\Phi_{ohm,a}$: ohmic heat source term at the anode (W m^{-3})
$\Phi_{ohm,c}$: ohmic heat source term at the cathode (W m^{-3})
Φ_{φ}: potential source term (A m^{-3})
$\Delta S_{cathode}$: entropy change of the half cathode cell reaction (J mol^{-1} K^{-1})
ΔS_{anode}: entropy change of the half anode cell reaction (J mol^{-1} K^{-1})
$\Delta S_{overall}$: entropy change of the overall reaction (J mol^{-1} K^{-1})
r_1: power of CO_2 partial pressure for exchange current density in cathode
r_2: power of O_2 partial pressure for exchange current density in cathode
T: operating temperature (K)
u: x-direction velocity (m s^{-1})
V_{cell}: working voltage (V)
V_{th}: open circuit voltage of the DCFC (V)
v: y-direction velocity (m s^{-1})
X: height of the DCFC (m)
Y: length of the DCFC (m)
y_i: molar fraction of species i
Z: width of the DCFC (m)

Greek letters
α_a: anode charge transfer coefficient
α_c: cathode charge transfer coefficient
ε: porosity
ρ: mixture density (kg m^{-3})
$\eta_{act,e}$: activation overpotential of the electrode (anode, cathode) (V)
σ_c: conductivity coefficient of the anode (S m^{-1})
σ_{elec}: conductivity coefficient of the electrolyte (S m^{-1})
σ_{cat}: conductivity of the cathode (S m^{-1})
μ: mixture kinematical viscosity (PI)
φ: potential (V)
λ: thermal conductivity of the mixture (W m^{-1} K^{-1})
λ_s: solid thermal conductivity (W m^{-1} K^{-1})
λ_f: fluid thermal conductivity (W m^{-1} K^{-1})